# Thermodynamics of Self Assembly and Supramolecular Transitions using Enhanced Sampling

Zhitong Jiang,[†] Zachariah Vicars,[†] Suruchi Fialoke,[†] Sumanth N. Jamadagni,[‡] Peter H. Koenig,[‡] and Amish J. Patel[*,†]

†*Department of Chemical and Biomolecular Engineering, University of Pennsylvania, Philadelphia, PA 19104, USA*

‡*The Procter & Gamble Company, Mason, Ohio 45040, USA*

E-mail: amish.patel@seas.upenn.edu

**Abstract**

Computational studies of self-assembly have the potential to provide rich insights into their underlying thermodynamics and identify optimal system conditions for applications, such as nanomaterial synthesis or drug delivery. However, both self-assembly and supramolecular transitions can be hindered by free energy barriers, rendering them rare events on molecular timescales and making it challenging to sample them. Here, we show that the use of enhanced sampling techniques, when combined with a judiciously chosen set of order parameters, offers an efficient and robust route for characterizing the thermodynamics of self-assembly and supramolecular transitions. Specifically, we show that transitions between states with different periodicities or symmetries can be reversibly sampled by biasing a relatively small number of Fourier components of the particle density. We illustrate our approach by computing the free energy required to cleave a liquid slab and estimating the corresponding liquid-vapor surface tension. We also characterize the free energetics of the transition between spherical and rod-shaped droplets. These results serve as a first step towards the development of a systematic computational framework for exploring transitions in diverse supramolecular systems, such as surfactants or block copolymers, and characterizing the thermodynamics of their self-assembly.

# Introduction

The organization of molecular building blocks, such as surfactants, peptides or block copolymers, into self-assembled structures, such as micelles, condensates or ordered mesophases, plays an important role in a diverse disciplines,[1–6] ranging from soft matter and nanotechnology[7–14] to interface science and biophysics.[15–18] Consequently, both experimental and computational techniques have sought to better understand the molecular driving forces that underpin self-assembly.[19–23] In addition to monomer chemistry[24,25] and shape,[26–28] self-assembly can also be influenced by collective solvation effects.[29–33] Moreover, small changes

in system properties, such as temperature or pH, can trigger supramolecular transitions from one self-assembled mesophase to another.[34–38] Thus, being able to design systems that self-assemble into desired structures and identifying the conditions under which self-assembly can be carried out in a reproducible and/or tunable manner remains a grand challenge.[39–45]

In addition to predicting and controlling the supramolecular structure of a system, knowledge of the robustness and stability of such nano-scale phases is especially important in the manufacture of low-cost, industrial materials. In these applications, manufacturers want to maintain control over the material properties and prevent failure (e.g. unexpectedly crossing a phase boundary) when control over the feedstock and manufacturing process is heavily constrained. Accomplishing this experimentally can be impractical, as it may take weeks or months for supramolecular transitions to occur. Consequently, the use of modeling tools to quantify the proximity to phase transitions and alternate microstructures could help with assessing the risks of such failures.

Molecular simulations offer the promise of uncovering the complex relationships between the molecular characteristics of the building blocks (e.g., surfactants) and the self-assembled structures they might form (e.g., micelles) as well as the conditions under which such assembly might occur (e.g., critical micelle concentration). In particular, all-atom molecular dynamics (MD) simulations with explicit consideration of solvent have become increasingly adept at accurately capturing the molecular interactions that drive self-assembly. Moreover, such simulations are also transferable, and can be used to explore how subtle changes in solvent conditions[46–49] as well as surfactant architecture[50–52] or chemistry[53,54] influence self-assembly. However, all-atom explicit-solvent MD simulations can be computationally expensive, especially when the presence of free energy barriers renders self-assembly and/or supramolecular transitions rare events on molecular timescales.[55–58] Consequently, the vast majority of computational studies of self-assembly have employed coarse-grained approaches,[32,59–63] such as dissipative particle dynamics (DPD)[24,64–67] or self-consistent field theory (SCFT).[68–70] Such coarse-grained approaches provide a computationally efficient al-

ternative to atomistic simulations, and by facilitating exploration of the space of monomer chemistry (e.g., polarity) and/or system conditions (e.g, temperature), they can provide important insights into the physics of self-assembly.

Both all-atom and coarse-grained approaches would benefit from the development of methods for characterizing the free energetics of self-assembly and/or supramolecular transitions.[71–73] In principle, enhanced sampling techniques, such as umbrella sampling or metadynamics,[74–77] can facilitate the sampling of rare self-assembly or supramolecular transition events and the characterization of the underlying free energy landscapes. However, such techniques require the identification of robust order parameters that can be biased to reversibly sample the transition of interest.[26,72] Order parameters, such as radius of gyration,[78] aggregation number,[79] and similar such quantities,[80,81] have been used for studying self-assembly, and shape matching functions that capture the salient features of self-assembled structures have also been used to define order parameters.[82–84] However, a versatile set of order parameters that can be deployed to study the vast array of complex supramolecular structures[85] associated with polymer and surfactant self assembly remains elusive.

To address this challenge, here we explore the use of order parameters based on Fourier transforms of particle densities, which have been used extensively for nanostructure characterization ,[84,86–92] but seldom for enhanced sampling.[93,94] As most self-assembled structures possess simple, periodic motifs, their density and/or composition profiles can be succinctly described using a small set of wavevectors. We thus hypothesize that the transition between two different morphological states can be studied by identifying the Fourier components that vary most between the two states, and biasing the Fourier amplitudes of the most pertinent wave vectors. To test this hypothesis, here we study a series of increasingly complex model systems. We first illustrate our approach by studying the clustering of ideal gas particles, then study the rupturing of a Lennard-Jones liquid slab, and finally investigate the transition between spherical and cylindrical droplets. In each case, we are able to reversibly sample the transition of interest, characterize the underlying free energy landscape, and shed light on

the transition pathway. Our work uncovers important heuristics for accurately and efficiently sampling morphological transitions in self-assembled systems, and paves the way for a robust and generalizable framework for computational studies of self-assembly and supramolecular transitions.

# Methods

## Theory

### Fourier components of the particle density field

For a system with $N$ particles, the particle density field is defined as:

$$\rho(\mathbf{r}; \{\mathbf{r}_p\}) = \sum_{p=1}^{N} \delta(\mathbf{r} - \mathbf{r}_p), \tag{1}$$

where $\mathbf{r}_p$ is the position of the $p$th particle and $\delta$ stands for the Dirac delta function. The Fourier transform of the particle density field is given by:

$$\hat{\rho}_{\mathbf{k}} \equiv \mathcal{F}[\rho(\mathbf{r})] = \int_V \mathrm{d}\mathbf{r} \rho(\mathbf{r}) \exp\left(-i\mathbf{k} \cdot \mathbf{r}\right) \tag{2}$$

where $\mathbf{k}$ is the wave vector and the integral is performed over the simulation box volume, $V$. For cuboidal systems with periodic boundary conditions, $\hat{\rho}_{\mathbf{k}}$ takes on non-zero values only for $\mathbf{k} = (2\pi n_x/L_x, 2\pi n_y/L_y, 2\pi n_z/L_z)$, where $n_x$, $n_y$ and $n_z$ are integers and $L_x$, $L_y$ and $L_z$ are the lengths of the simulation box in the corresponding directions.

The particle density field can be expressed as a plane-wave basis-set expansion using the Fourier amplitudes, $\hat{\rho}_{\mathbf{k}}$, (inverse Fourier transform) as follows:

$$\rho(\mathbf{r}) = \frac{1}{V} \sum_{\mathbf{k}} \hat{\rho}_{\mathbf{k}} \exp\left(i\mathbf{k} \cdot \mathbf{r}\right) \tag{3}$$

Using Euler's formula, $\hat{\rho}_{\mathbf{k}}$ can be decomposed into real and imaginary components as:

$$\hat{\rho}_{\mathbf{k}} = \hat{\rho}_{\mathbf{k},\Re} + i\hat{\rho}_{\mathbf{k},\Im}, \tag{4}$$

with the components being given by:

$$\hat{\rho}_{\mathbf{k},\Re} = \sum_{p=1}^{N} \cos\left(\mathbf{k}\cdot\mathbf{r}_p\right) \quad , \quad \hat{\rho}_{\mathbf{k},\Im} = -\sum_{p=1}^{N} \sin\left(\mathbf{k}\cdot\mathbf{r}_p\right) \tag{5}$$

**Bias Potentials**

To reversibly transition between configurations with different periodicities or symmetries, here we independently bias the real, $\hat{\rho}_{\mathbf{k},\Re}$, and imaginary, $\hat{\rho}_{\mathbf{k},\Im}$, components of $\hat{\rho}_{\mathbf{k}}$, such that our biasing potential, $U_{\mathbf{k}}(\hat{\rho}_{\mathbf{k}})$, can be written as:

$$U_{\mathbf{k}}(\hat{\rho}_{\mathbf{k}}) = U_{\mathbf{k},\Re}(\hat{\rho}_{\mathbf{k},\Re}) + U_{\mathbf{k},\Im}(\hat{\rho}_{\mathbf{k},\Im}), \tag{6}$$

with $U_{\mathbf{k},\Re}(\hat{\rho}_{\mathbf{k},\Re})$ and $U_{\mathbf{k},\Im}(\hat{\rho}_{\mathbf{k},\Im})$ chosen to be harmonic functions:

$$\begin{aligned} U_{\mathbf{k},\Re}(\hat{\rho}_{\mathbf{k},\Re}) &= \frac{\kappa_{\mathbf{k},\Re}}{2}(\hat{\rho}_{\mathbf{k},\Re} - \hat{\rho}^*_{\mathbf{k},\Re})^2, \text{ and} \\ U_{\mathbf{k},\Im}(\hat{\rho}_{\mathbf{k},\Im}) &= \frac{\kappa_{\mathbf{k},\Im}}{2}(\hat{\rho}_{\mathbf{k},\Im} - \hat{\rho}^*_{\mathbf{k},\Im})^2, \end{aligned} \tag{7}$$

where the spring constants, $\kappa_{\mathbf{k},\Re}$ and $\kappa_{\mathbf{k},\Im}$ as well as the set-points, $\hat{\rho}^*_{\mathbf{k},\Re}$ and $\hat{\rho}^*_{\mathbf{k},\Im}$, are user-specified parameters, chosen according to the rules of thumb described in refs.[95,96] When it is desirable to bias the $\hat{\rho}_{\mathbf{k},\Re}$ and/or $\hat{\rho}_{\mathbf{k},\Im}$-values of multiple wavevectors, $\{\mathbf{k}_i\}$, the overall biasing potential is obtained by simply adding the biasing potentials for the pertinent wavevectors, $U = \sum_{\mathbf{k}_i} U_{\mathbf{k}_i}$. Because $\hat{\rho}_{\mathbf{k},\Re}$ and $\hat{\rho}_{\mathbf{k},\Im}$ are continuous and differentiable functions of the particle positions (Equation 5), the force, $\mathbf{f}_{\mathbf{k}p}$, on the $p^{\text{th}}$ particle, arising from the bias on

$\hat{\rho}_{\mathbf{k}}$ can be readily obtained as follows:

$$\begin{aligned}
\mathbf{f}_{\mathbf{k}p} &= -\nabla_p U_{\mathbf{k}}(\hat{\rho}_{\mathbf{k}}) \\
&= -\nabla_p U_{\mathbf{k},\Re}(\hat{\rho}_{\mathbf{k},\Re}) - \nabla_p U_{\mathbf{k},\Im}(\hat{\rho}_{\mathbf{k},\Im}) \\
&= -\kappa_{\mathbf{k},\Re}(\hat{\rho}_{\mathbf{k},\Re} - \hat{\rho}^*_{\mathbf{k},\Re})\nabla_p \hat{\rho}_{\mathbf{k},\Re} - \kappa_{\mathbf{k},\Im}(\hat{\rho}_{\mathbf{k},\Im} - \hat{\rho}^*_{\mathbf{k},\Im})\nabla_p \hat{\rho}_{\mathbf{k},\Im} \\
&= \left[\kappa_{\mathbf{k},\Re}(\hat{\rho}_{\mathbf{k},\Re} - \hat{\rho}^*_{\mathbf{k},\Re}) \sin(\mathbf{k}\cdot\mathbf{r}_p) + \kappa_{\mathbf{k},\Im}(\hat{\rho}_{\mathbf{k},\Im} - \hat{\rho}^*_{\mathbf{k},\Im}) \cos(\mathbf{k}\cdot\mathbf{r}_p)\right] \mathbf{k}. \qquad (8)
\end{aligned}$$

Thus, $\mathbf{f}_{\mathbf{k}p}$ acts in the direction of $\mathbf{k}$. To exercise control over $\rho(\mathbf{r})$ and drive the system towards increasingly complex configurations, we can bias the Fourier amplitudes, $\hat{\rho}_{\mathbf{k}}$, of multiple wavevectors, with the total force, $\mathbf{f}_p$, on the $p^{\text{th}}$ particle being $\mathbf{f}_p = \sum_{\mathbf{k}} \mathbf{f}_{\mathbf{k}p}$.

In each of the processes we study here, the pertinent configurations possess reflection symmetry around the center of the simulation box, which implies that the average particle density can be expressed solely as a sum of even functions. Consequently, $\hat{\rho}_{\mathbf{k},\Im}$ is expected to be zero, on average, for all $\mathbf{k}$, and biasing $\hat{\rho}_{\mathbf{k},\Re}$ is sufficient to exercise control over the average density field (Equation 5). To restrain configurations sampled in our biased simulations to obey reflection symmetry, for every $\hat{\rho}_{\mathbf{k},\Re}$ that we bias, we include a harmonic bias on $\hat{\rho}_{\mathbf{k},\Im}$ with a set-point, $\hat{\rho}^*_{\mathbf{k},\Im}$, of 0 and a spring constant, $\kappa_{\mathbf{k},\Im} = \kappa_{\mathbf{k},\Re}$ (Equation 7).

To sample $\hat{\rho}_{\mathbf{k},\Re}$-values spanning the range of interest, we perform a series of biased simulations by systematically varying $\hat{\rho}^*_{\mathbf{k},\Re}$. To obtain the corresponding free energy profile, e.g., $F(\hat{\rho}_{\mathbf{k},\Re})$, we then employ the Weighted Histogram Analysis Method (WHAM).[97–99] When biasing along multiple wave vectors, $\{\mathbf{k}_i\}$, we choose to sample along a linear path in the high dimensional space of $\{\hat{\rho}_{\mathbf{k}_i,\Re}\}$. In particular, to sample the transition between initial and final configurations defined by $\{\hat{\rho}^0_{\mathbf{k}_i,\Re}\}$ and $\{\hat{\rho}^1_{\mathbf{k}_i,\Re}\}$, respectively, we define the variable $\lambda^*$ that linearly interpolates between the two configurations. For every wave-vector that we bias, the set-point, $\hat{\rho}^*_{\mathbf{k}_i,\Re}(\lambda^*) = \hat{\rho}^0_{\mathbf{k}_i,\Re} + \lambda^* \cdot (\hat{\rho}^1_{\mathbf{k}_i,\Re} - \hat{\rho}^0_{\mathbf{k}_i,\Re})$, is chosen such that configurations consistent with $\{\hat{\rho}^0_{\mathbf{k}_i,\Re}\}$ are preferred when $\lambda^* = 0$, whereas those with $\{\hat{\rho}^1_{\mathbf{k}_i,\Re}\}$ are preferred as $\lambda^* \to 1$. In other words, the total bias potential, $U_{\kappa_\Re,\lambda^*} = \sum_{\mathbf{k}_i} \frac{\kappa_\Re}{2}[\hat{\rho}_{\mathbf{k}_i,\Re} - \hat{\rho}^*_{\mathbf{k}_i,\Re}(\lambda^*)]^2$.

To quantify how far along the high-dimensional linear pathway each configuration in our biased simulations sits, we introduce the order parameter, $\lambda$, which depends on $\{\hat{\rho}_{\mathbf{k}_i,\Re}\}$ and is defined as follows:

$$\lambda(\{\hat{\rho}_{\mathbf{k}_i,\Re}\}) = \frac{\sum_i (\hat{\rho}_{\mathbf{k}_i,\Re} - \hat{\rho}^0_{\mathbf{k}_i,\Re}) \cdot (\hat{\rho}^1_{\mathbf{k}_i,\Re} - \hat{\rho}^0_{\mathbf{k}_i,\Re})}{\sum_i (\hat{\rho}^1_{\mathbf{k}_i,\Re} - \hat{\rho}^0_{\mathbf{k}_i,\Re})^2} \tag{9}$$

We estimate the change in free energy along the linear path $F(\lambda)$, using WHAM.[97–99]

## Simulation Details

All simulations are performed using the GROMACS package (version 4.5.3) ,[100] suitably modified to incorporate the required biases. The leap frog algorithm [101] was used to integrate the equations of motion with a 2 fs time-step; the center of mass motion was removed and the neighbor list was updated every time-step. Periodic boundary conditions were employed in all directions. The atoms were chosen to have a mass of 16.04 amu, and Lennard-Jones (LJ) interaction parameters of $\sigma = 0.373$ nm and $\epsilon = 1.23047$ kJ/mol were used; LJ interactions were truncated at $4\sigma$. All simulations are performed in the NVT ensemble. The system temperature was maintained using the canonical velocity-rescaling thermostat [102] with a time constant of 0.5 ps. Additional system-specific details are provided below.

**Ideal systems** A cubic simulation box that is 10 nm in each direction is populated with 20 non-interacting particles. The system is simulated at 148 K. All simulation runs are performed for two 2 ns, with the first 0.2 ns discarded as equilibration time. For the wave vector, $\mathbf{k} = (0, 0, 2\pi/L_z)$, we sample the entire range of $\hat{\rho}_{\mathbf{k},\Re}$ using 13 biased simulations that employ harmonic biasing potentials with a fixed spring constant, $\kappa_{\mathbf{k},\Re} = 0.2$ kJ/mol, and different values of $\hat{\rho}^*_{\mathbf{k},\Re}$, equally spaced from $-30$ to 30.

**Cleaving LJ Slabs** A cuboidal simulation box that is 5 nm long in the $x$- and $y$-directions and 30 nm in the $z$-direction is initialized with 4500 LJ particles. The temperature is set to 148 K. After equilibration, a liquid slab forms in the center of the box with liquid-

vapor interfaces that are orthogonal to the $z$ direction (Figure 2a, top). From this unbiased simulation, we obtain the density profile for the one-slab configuration with its center of mass pegged to the center of the box (Figure 2b); the density profile is then fit using tanh functions, which capture its sigmoidal behavior. The one-slab density profile is also used to infer the corresponding two-slab density profile assuming that each slab has half the number of LJ particles and that the interface shapes are not affected by the cleaving of the slabs (Figure 2b). To compare two sets of density profiles, $\rho_1(z)$ and $\rho_2(z)$, we define a root mean squared deviation (RMSD) as follows:

$$\mathrm{RMSD} = \frac{1}{\rho_l}\sqrt{\frac{1}{L_z}\int_0^{L_z}\Big[\rho_1(z) - \rho_2(z)\Big]^2 \mathrm{d}z} \tag{10}$$

where $\rho_l$ is the bulk liquid density.

The last frame of the equilibrium simulation is used as an initial configuration for the biased simulations. To sample the transition between one-slab and two-slab configurations, the linear biasing variable, $\lambda^*$, is systematically varied from -0.1 and 1.1 using 25 windows, and $\kappa_{\Re}$ is chosen to be 0.001 kJ/mol for all wavevectors. We also carried out a parallel set of biased simulations, initialized in the two-slab configuration, to interrogate whether the free energy profiles display hysteresis. All biased simulations are run for 2 ns, with the first 0.5 ns being discarded for equilibration. To estimate the surface tension at different temperatures, similar calculations are performed at 162.8 K and 125.8 K.

When computing the surface tension, we use a thermodynamic cycle with legs that feature the biasing potential, $U_{\kappa_{\Re},\lambda^*} = \sum_{\mathbf{k}_i} \frac{\kappa_{\Re}}{2}[\hat{\rho}_{\mathbf{k}_i,\Re} - \hat{\rho}^*_{\mathbf{k}_i,\Re}(\lambda^*)]^2$, being turned on in the one-slab configuration ($\lambda^* = 0$) and turned off in the two-slab configuration ($\lambda^* = 1$). To compute the free energy of turning on the biasing potential, we use thermodynamic integration:[96,103,104]

$$\Delta F_1 = \int_0^{\kappa_{\Re}} \Big(\frac{\partial F_{\kappa,\lambda^*=0}}{\partial \kappa}\Big)\mathrm{d}\kappa \tag{11}$$

where $F_{\kappa,\lambda^*}$ is the free energy of the system in a biased ensemble with a bias potential, $U_{\kappa,\lambda^*}$,

and $\partial F_{\kappa,\lambda^*=0}/\partial\kappa = \langle \sum_{\mathbf{k}_i} \frac{1}{2}[\hat{\rho}_{\mathbf{k}_i,\Re} - \hat{\rho}^*_{\mathbf{k}_i,\Re}(\lambda^*=0)]^2 \rangle_{\kappa,\lambda^*=0}$ is estimated from biased simulations. Similarly, we compute the free energy of turning off the biasing potential as:

$$\Delta F_3 = -\int_0^{\kappa_\Re} \left(\frac{\partial F_{\kappa,\lambda^*=1}}{\partial\kappa}\right) \mathrm{d}\kappa \tag{12}$$

where $\partial F_{\kappa,\lambda^*=1}/\partial\kappa = \langle \sum_{\mathbf{k}_i} \frac{1}{2}[\hat{\rho}_{\mathbf{k}_i,\Re} - \hat{\rho}^*_{\mathbf{k}_i,\Re}(\lambda^*=1)]^2 \rangle_{\kappa,\lambda^*=1}$. To prevent slabs from coalescing during the process of turning off the biasing potential, we additionally employ a well potential, $U_{\text{well}}$, that penalizes large excursions away from the two-basin configuration, but does not bias small fluctuations within the basin; only configurations with $U_{\text{well}} = 0$ are included when computing the ensemble averages, $\langle \ldots \rangle_{\kappa,\lambda^*=1}$. Additional details pertaining to the definition and use of $U_{\text{well}}$ are included in the SI.

**Changing Droplet Shapes** By judiciously choosing the net particle density, we situate our system at a point in phase space where both cylindrical and spherical droplets are (meta)stable.[105] In particular, we randomly place 9000 LJ particles in a cubic box with a side of 15 nm and run several simulations to let the system equilibrate at 148K. Following equilibration, either cylindrical or spherical droplets are observed, providing us with initial configurations for our biased simulations. To sample the transition between spherical and cylindrical droplets, the linear biasing variable, $\lambda^*$, is systematically varied from -0.1 and 1.2, and $\kappa_\Re$ is chosen to be 0.0002 kJ/mol for all wavevectors. Each biased simulation was run for 5 ns with the first 1 ns being discarded for equilibration.

# Results and Discussion

## Ideal system

To illustrate our approach, we first characterize the free energetics, $F(\hat{\rho}_{\mathbf{k},\Re})$, for a system of ideal gas particles, for which thermodynamic averages can be computed analytically and compared to our simulation results. In particular, we study a system with 20 ideal particles

in a cubic box (Figure 1a), as detailed in the Methods section, and seek to characterize $F(\hat{\rho}_{\mathbf{k},\Re})$ for the wave-vector, $\mathbf{k} = (0, 0, 2\pi/L_z)$. The free energetics obtained from an unbiased simulation (Figure 1b, blue line), highlight that $F(\hat{\rho}_{\mathbf{k},\Re})$ displays a minimum at $\hat{\rho}_{\mathbf{k},\Re} = 0$ and it is symmetric around its minimum. Because an ideal gas must, on average, have a uniform particle density field, particle density waves with a positive amplitude, $\hat{\rho}_{\mathbf{k},\Re}$, should indeed occur with the same likelihood as the corresponding waves with a negative amplitude (for all wavevectors). We also find that the distribution of $\hat{\rho}_{\mathbf{k},\Re}$ near its mean is Gaussian (Figure 1b, black dashed line) with a variance, $\langle \delta\hat{\rho}^2_{\mathbf{k},\Re} \rangle = N/2$; as shown in the SI, these findings are also in line with our expectations for an ideal gas.

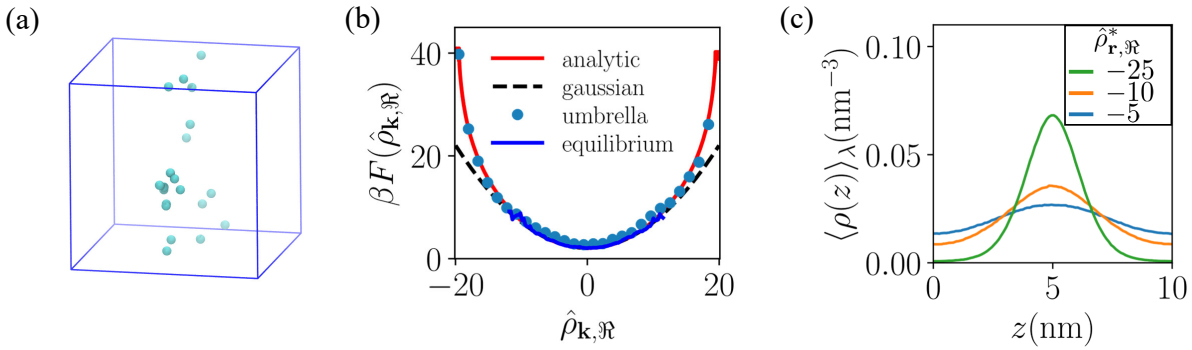


Figure 1: Illustration of our approach using an ideal gas system. (a) A biased simulation snapshot of a system comprised of $N = 20$ ideal particles in a cubic box. (b) The free energetics, $F(\hat{\rho}_{\mathbf{k},\Re})$, of the ideal system for the wave vector $\mathbf{k} = (0, 0, 2\pi/L_z)$ are shown. The data obtained from an unbiased simulation (solid blue line) suggests that $F(\hat{\rho}_{\mathbf{k},\Re})$ is parabolic (black dashed line) near $\hat{\rho}_{\mathbf{k},\Re} = 0$, highlighting that $\hat{\rho}_{\mathbf{k},\Re}$ obeys Gaussian statistics near its mean, $\langle \hat{\rho}_{\mathbf{k},\Re} \rangle = 0$. Estimates of $F(\hat{\rho}_{\mathbf{k},\Re})$, obtained over the entire range of $\hat{\rho}_{\mathbf{k},\Re}$ using umbrella sampling (blue circles), agree with the unbiased estimates near $\hat{\rho}_{\mathbf{k},\Re} = 0$, but display significant deviation from parabolic behavior as $\hat{\rho}_{\mathbf{k},\Re}$ approaches $\pm N$. Such deviation is consistent with the analytical form of $F(\hat{\rho}_{\mathbf{k},\Re})$ expected for an ideal gas (solid red line). (c) The average particle density profiles, $\langle \rho(z) \rangle_{\kappa,\hat{\rho}^*_{\mathbf{k},\Re}}$, obtained from three biased simulations with different values of the bias set-point, $\hat{\rho}^*_{\mathbf{k},\Re}$, are shown, highlighting that negative $\hat{\rho}^*_{\mathbf{k},\Re}$-values lead to enhanced particle densities at the center of the box.

We now seek to sample $\hat{\rho}_{\mathbf{k},\Re}$-values far from its mean, $\langle \hat{\rho}_{\mathbf{k},\Re} \rangle = 0$, by employing a harmonic biasing potential, $\frac{1}{2}\kappa(\hat{\rho}_{\mathbf{k},\Re} - \hat{\rho}^*_{\mathbf{k},\Re})^2$, with spring constant, $\kappa$, and set-point, $\hat{\rho}^*_{\mathbf{k},\Re}$, as discussed in the Methods section. To shed light on how the biasing potential influences the real-space particle density, we plot the average particle density, $\langle \rho(z) \rangle_{\kappa,\hat{\rho}^*_{\mathbf{k},\Re}}$, in biased ensembles with select values of $\hat{\rho}^*_{\mathbf{k},\Re}$ (Figure 1c). In the presence of biasing potential with negative values of

the set-point, $\hat{\rho}^*_{\mathbf{k},\Re}$, we observe an accumulation of particles at the center of the simulation box. To understand this observation, we use the inverse Fourier transform (Equation 3) to relate the average real-space density, $\langle\rho(z)\rangle_{\kappa,\hat{\rho}^*_{\mathbf{k},\Re}}$, to the corresponding averages, $\langle\hat{\rho}_{\mathbf{k},\Re}\rangle_{\kappa,\hat{\rho}^*_{\mathbf{k},\Re}}$, of the Fourier amplitudes: $\langle\rho(z)\rangle_{\kappa,\hat{\rho}^*_{\mathbf{k},\Re}} = \frac{N}{V} + \frac{2}{V}\sum_{\mathbf{k}'\neq 0}\langle\hat{\rho}_{\mathbf{k}',\Re}\rangle_{\kappa,\hat{\rho}^*_{\mathbf{k},\Re}}\cos(\mathbf{k}'\cdot\mathbf{r})$. If we assume that the average Fourier amplitudes, $\langle\hat{\rho}_{\mathbf{k}',\Re}\rangle_{\kappa,\hat{\rho}^*_{\mathbf{k},\Re}}$, for wavevectors that were not biased ($\mathbf{k}' \neq \mathbf{k}$) are unaffected by the bias, i.e., $\langle\hat{\rho}_{\mathbf{k}'\neq\mathbf{k},\Re}\rangle_{\kappa,\hat{\rho}^*_{\mathbf{k},\Re}} \approx 0$, then: $\langle\rho(z)\rangle_{\kappa,\hat{\rho}^*_{\mathbf{k},\Re}} \approx \frac{N}{V} + \frac{2}{V}\langle\hat{\rho}_{\mathbf{k},\Re}\rangle_{\kappa,\hat{\rho}^*_{\mathbf{k},\Re}}\cos\left(\frac{2\pi z}{L_z}\right)$. Additionally, given that the unbiased average, $\langle\hat{\rho}_{\mathbf{k},\Re}\rangle = 0$, we expect negative $\hat{\rho}^*_{\mathbf{k},\Re}$-values to result in $\langle\hat{\rho}_{\mathbf{k},\Re}\rangle_{\kappa,\hat{\rho}^*_{\mathbf{k},\Re}} < 0$. Thus, regions with negative $\cos\left(\frac{2\pi z}{L_z}\right)$, i.e., near the center of the box, should have particle densities that are greater $N/V$. Conversely, positive values of $\hat{\rho}^*_{\mathbf{k},\Re}$ should drive particles towards the edges of the box.

As described in the Methods section, by performing biased simulations that enable us to sample a wide range of $\hat{\rho}_{\mathbf{k},\Re}$-values, we then compute the free energy profiles, $F(\hat{\rho}_{\mathbf{k},\Re})$, over the entire range of $\hat{\rho}_{\mathbf{k},\Re}$, from $-N$ to $N$. The free energy profile, shown in Figure 1b (filled circles) is parabolic near the mean, as expected from our unbiased simulation, but sharpens towards the tails such that at $\beta F(\hat{\rho}_{\mathbf{k},\Re} = \pm N) = 2N$. By leveraging the simplicity of the ideal gas system, we derive an analytical expression for $F(\hat{\rho}_{\mathbf{k},\Re})$ (details included in SI), and as shown in Figure 1b (red line), our simulated estimates of $F(\hat{\rho}_{\mathbf{k},\Re})$ are in excellent agreement with analytical free energy expression.

## Cleaving a liquid slab

The coalescence and/or cleavage of liquid droplets or vapor bubbles plays an important role in a variety of fields, ranging from the construction of microfluidic devices,[106] emulsions for drug delivery,[107] and in drop-wise condensation heat transfer.[108] Here we seek to reversibly cleave a Lennard-Jones liquid slab along the $xy$-plane to create two liquid slabs separated in the $z$-direction (Fig. 2a). We leverage the fact that these configurations differ in their periodicities and should therefore also differ in the wavevectors that dominate the Fourier transform of their average density profiles (Fig. 2b). Indeed, as shown in Fig. 2c, the Fourier

amplitudes, $\langle\hat{\rho}_{\mathbf{k},\Re}\rangle$, in the one-slab and two-slab states are dominated by the $n_z = 1$ and $n_z = 2$ wavevectors, respectively. To quantify the contribution of the higher $n_z$ wavevectors to the overall density profile, we systematically increase the number of wave-vectors, $N_w$, included in the Fourier expansion (Equation 4):

$$\rho_{N_w}(z) = \frac{N}{V} + \frac{2}{V}\sum_{n_z=1}^{N_w} \hat{\rho}_{\mathbf{k},\Re} \cos\left(\frac{2\pi n_z}{L_z} z\right) \ , \ \mathbf{k} = (0, 0, 2\pi n_z/L_z), \tag{13}$$

and compare the resulting truncated density profiles against the full density profiles using a root mean squared deviation (RMSD) metric (Equation 10). Figure 2d shows that as $N_w$ increases, the resulting RMSD decreases exponentially for both configurations, and that $N_w = 12$ wavevectors are sufficient to results in RMSD-values below 0.02.

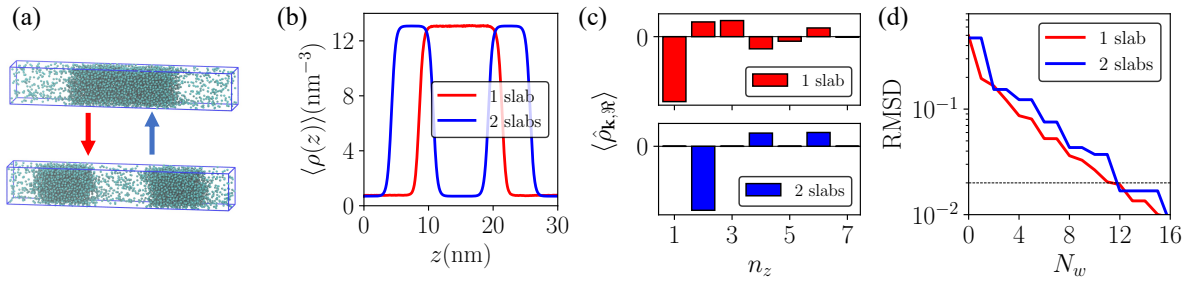


Figure 2: (a) Simulation snapshots in the one-slab (top) and two-slab (bottom) states. The simulation box is shown using blue lines and the Lennard-Jones particles are shown as cyan spheres. (b) Average density profiles are shown along the $z$-direction for the one- and two-slab states. (c) For both the one- and two-slab states, the average Fourier amplitudes, $\langle\hat{\rho}_{\mathbf{k},\Re}\rangle$, are shown for the first 7 wavevectors, $\mathbf{k} = (0, 0, 2\pi n_z/L_z)$, where $n_z = 1, 2 \ldots 7$. (d) The root mean square deviation (RMSD) between the truncated and actual density profiles is shown as a function of the number of wavevectors, $N_w$, for the one- and two-slab states.

To cleave the slab, we thus choose to bias the Fourier amplitudes, $\hat{\rho}_{\mathbf{k},\Re}$, of the first 12 wavevectors. In particular, we carry out a set of biased simulations wherein the $\hat{\rho}_{\mathbf{k},\Re}$-values for each of the 12 wavevectors are varied in a concerted manner along a linear pathway connecting the two basins, as described in the Methods section. Initializing our system in the one-slab configuration, we perform a total of 25 biased simulations, varying the linear biasing parameter, $\lambda^*$, from -0.10 to 1.10, where $\lambda^*$-values of 0 and 1 seek to localize the system in the one- and two-slab states, respectively. We denote this set of simulations as

the "forward" sampling path and analyze them to obtain the free energy profile, $F(\lambda)$, for transitioning the system from the one-slab to the two-slab configuration (Figure 3a, solid red line). The profile, $F(\lambda)$, displays two basins at $\lambda = 0$ (stable) and $\lambda = 1$ (metastable), which are separated by a relatively large free energy barrier, and the free energy difference between the two basins is roughly 175 $k_{\mathrm{B}}T$. To interrogate our ability to reversibly sample $F(\lambda)$ by biasing the Fourier amplitudes, $\hat{\rho}_{\mathbf{k},\Re}$, we repeat the entire set of umbrella sampling calculations using the two-slab configuration as our initial configuration, and denote this set as "backward" sampling simulations. The free energy profile, $F(\lambda)$, obtained from the backward simulations are shown in Figure 3a (blue dashed line) and agree well with the forward path results (solid, red line), suggesting that the sampling of the cleavage transition was not impeded by unanticipated orthogonal barriers.

To better understand how the transition proceeds along our prescribed path, we plot the average density profiles, $\langle \rho(z) \rangle_{\kappa,\lambda^*}$, obtained from our biased simulations in Figure 3b. As $\lambda^*$ is increased from 0 to 1, the average densities decrease at the center of the box and increase near its edges. Interestingly, for intermediate values of $\lambda^*$, the density profiles are not smooth, but instead display small "wiggles", i.e., high wavevector features. We posit that the density gradients underpinning these wiggles contribute to the large free energy barrier separating the basins, which in turn, necessitates the use of numerous biased windows to sample the transition pathway. To interrogate whether it might be possible to reversibly sample the cleavage transition along a path that presents smaller barriers to the transition (and is thereby more efficient to sample), we seek to exercise less control over the transition path by biasing fewer wavevectors. To this end, we now employ only the two characteristic wavevectors that dominate the one-slab ($n_z = 1$) and two-slab ($n_z = 2$) configurations, biasing along the linear pathway connecting the two basins in the $(\hat{\rho}_{\mathbf{k}_1,\Re}, \hat{\rho}_{\mathbf{k}_2,\Re})$ space. The corresponding free energy profiles, obtained from the forward and reverse simulations, are in excellent agreement with one another (Figure 3a), highlighting that the cleavage transition can be reversibly sampled by biasing only two wavevectors. Moreover, while the free energy

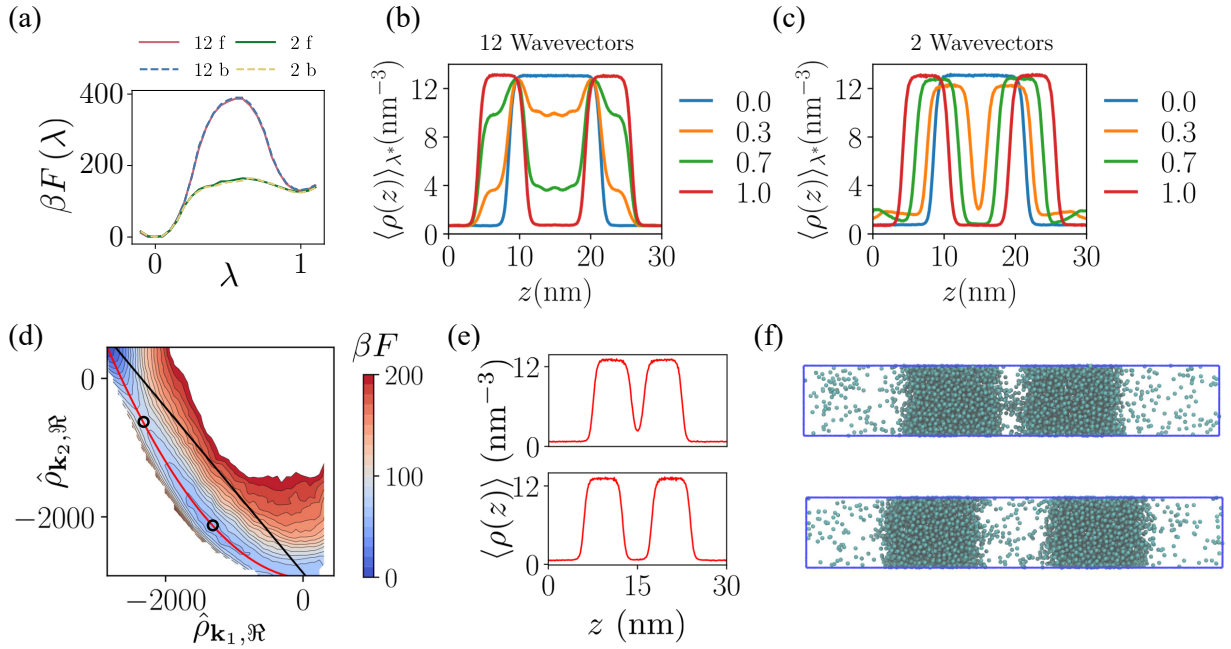


Figure 3: (a) The free energetics, $F(\lambda)$, of cleaving a liquid slab. The results obtained from biasing the Fourier amplitudes, $\hat{\rho}_{\mathbf{k},\Re}$, of 12 wave vectors are shown in red for rupturing the slab and in blue for coalescing the slabs; the corresponding results for biasing 2 Fourier amplitudes are shown in green and yellow, respectively. (b) Average density profiles obtained from simulations in which the Fourier amplitudes of 12 wave vectors are biased; density profiles corresponding to biased simulations with $\lambda^*$-values of 0, 0.3, 0.7 and 1 are shown. (c) Average density profiles obtained from simulations in which the Fourier amplitudes of 2 wave vectors are biased. (d) The two-dimensional free energy landscape, $F(\hat{\rho}_{\mathbf{k}_1,\Re}, \hat{\rho}_{\mathbf{k}_2,\Re})$, obtained by biasing the wavevectors, $\mathbf{k}_1 = (0, 0, 2\pi/L_z)$ and $\mathbf{k}_2 = (0, 0, 4\pi/L_z)$. The linear pathway connecting the one- and two-slab configurations (black line) as well as the minimum free energy path (red line) are shown. (e) Average density profiles and the corresponding (f) simulation snapshots are shown at select points along the minimum free energy path (denoted by circles in panel d): the saddle point (top) and the local minimum in the two-slab basin (bottom).

difference between the two-slab and one-slab basins that is obtained using simulations that bias 12 and 2 wavevectors is identical (as expected), the barrier separating the two basins is much smaller in the latter case, enabling more efficient sampling of the transition. As hypothesized, the average density profiles, $\langle\rho(z)\rangle_{\kappa,\lambda^*}$, obtained by biasing only 2 wavevectors (Figure 3c), are relatively smooth and do not show any high wavevector features.

To gain a deeper understanding into the cleavage transition pathway, we also compute the two-dimensional free energy landscape, $F(\hat{\rho}_{\mathbf{k}_1,\Re}, \hat{\rho}_{\mathbf{k}_2,\Re})$ (Figure 3d). The global minimum in free energy, corresponding to the one liquid slab configuration, is observed at small $\hat{\rho}_{\mathbf{k}_1,\Re}$

and large $\hat{\rho}_{\mathbf{k}_2,\Re}$ (top-left of Figure 3d), and a local minimum is observed at large $\hat{\rho}_{\mathbf{k}_1,\Re}$ and small $\hat{\rho}_{\mathbf{k}_2,\Re}$ near the two-slab configuration (bottom-right of Figure 3d). The minimum free energy path in the $(\hat{\rho}_{\mathbf{k}_1,\Re}, \hat{\rho}_{\mathbf{k}_2,\Re})$ space is also shown in Figure 3d (magenta), highlighting the curved path that offers the least resistance (i.e., barrier) to the cleavage transition, and its deviation from the linear path connecting the one- and two-slab configurations (solid, black line). The average particle density profiles at select states along the minimum free energy path are also shown (Figure 3e). In particular, at the saddle point, we observe two slabs connected with a small, liquid cylinder (Figure 3f). We note that the metastable basin in $F(\hat{\rho}_{\mathbf{k}_1,\Re}, \hat{\rho}_{\mathbf{k}_2,\Re})$ does not coincide with the two-slab configuration (even though both states feature two distinct slabs, Figures 3e,f) because the proximity of the two slabs and the resulting dispersion attractions between them makes the former slightly more favorable than the latter.

## Estimating Surface Tension

Surface tension, $\gamma$, plays a crucial role in driving a wide variety of self-assembly processes,[109–112] prompting the development of a number of simulation techniques for estimating this important quantity.[113–118] Because cleaving a liquid slab creates two new vapor-liquid interfaces, our ability to reversibly cleave the slab and quantify the corresponding free energetic cost, $\Delta F$, can be leveraged to estimate $\gamma$ using: $\Delta F = 2L_x L_y \gamma$. To accurately estimate the free energy, $\Delta F$, of transitioning the system from unconstrained one-slab to two-slab states, we use the thermodynamic cycle[119] shown in Figure 4a. We first turn on a biasing potential (using two wavevectors) that localizes the system in the one-slab state with associated free energy being denoted $\Delta F_1$. Then, we cleave the liquid slab, transitioning to the two-slab state; the corresponding free energy, estimated in the previous section, is denoted as $\Delta F_2$. Finally, we turn off the biasing potential to obtain the unconstrained two-slab state with the resulting free energy being $\Delta F_3$, so that: $\Delta F = \Delta F_1 + \Delta F_2 + \Delta F_3$.

We determine $\Delta F_1$ and $\Delta F_3$ at $T = 148$ K using thermodynamic integration, as described

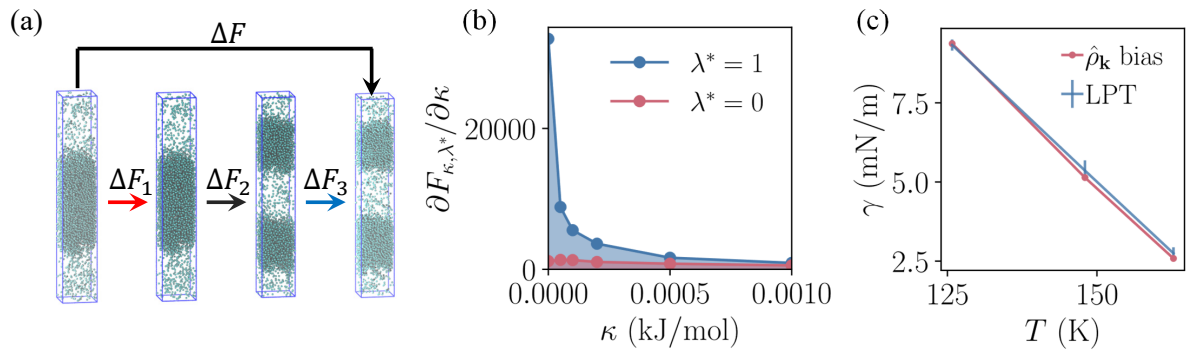


Figure 4: (a) Snapshots illustrating the thermodynamic circle for estimating surface tension. The biasing potential is first turned on, the Fourier space densities are biased to cleave the slab, and the bias is then turned off to obtained the final, cleaved configuration; lighter particle colors represent systems without the bias. (b) The thermodynamic force, $\partial F_{\kappa,\lambda^*}/\partial\kappa$, for systematically turning on the biasing potential in the one- and two-slab configurations; the area under the curve is the free energy for turning on the biasing potential. (c) Surface tension values obtained from this approach (red) agree well with the results obtained from the local pressure tensor (LPT, blue) method.

in the Methods section (Equations 11 and 12). The areas under the curves shown in Figure 4b provide us with estimates of $\Delta F_1 = 0.7\ k_\mathrm{B}T$ and $\Delta F_3 = -2.67\ k_\mathrm{B}T$. Because $\Delta F_1$ and $\Delta F_3$ are opposite in sign and similar in magnitude, and more importantly, because $\Delta F_2$ is much larger in magnitude than both $\Delta F_1$ and $\Delta F_3$, the total cleavage free energy, $\Delta F$, is largely determined by $\Delta F_2$. Using our estimate of $\Delta F$, we obtain the surface tension at $T = 148$ K to be 5.14 mN/m. We repeat these calculations at $T = 125.8$ K and 162.8 K and find that $\gamma$ decreases with increasing $T$, as expected (Figure 4c). We also estimate $\gamma$ using the local pressure tensor (LPT) method proposed by Irving and Kirkwood,[113,120] as described in the Supporting Information, and find that the two sets of $\gamma$-estimates are in excellent agreement with one another (Figure 4c).

## Transition between Spherical and Cylindrical Droplets

Amphiphilic molecules can self-assemble into micelles of different shapes, such as spheres, cylinders or disks, with the preferred morphology being a function of surfactant chemistry and concentration as well as solvent composition and temperature, among other variables. By modulating one or more of these variables, transitions between supramolecular assemblies

with different shapes can also be triggered. Indeed, increasing the surfactant concentration has been shown to result in a spherical to worm-like micelle transition.[121] However, such transitions can be rare events on molecular timescales making it challenging to study them using equilibrium simulations. To address this challenge, here we explore biasing Fourier components of the molecular density field, $\hat{\rho}_{\mathbf{k},\Re}$, to reversibly sample transitions between shapes with different symmetries. In particular, we illustrate our approach by studying the transition between spherical and cylindrical liquid droplets (Figure 5a).

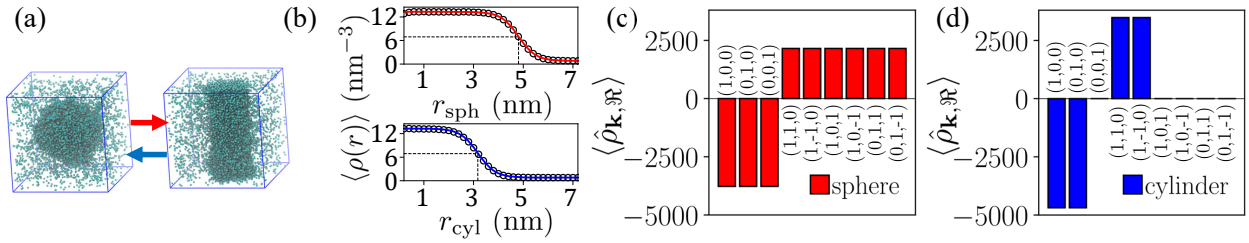


Figure 5: (a) Simulation snapshots of the system with spherical and cylindrical liquid droplets; LJ particles are shown as cyan spheres. (b) The average density profiles for the spherical and cylindrical droplets are shown as a function of the pertinent radial coordinate. For both the (c) spherical and (d) cylindrical droplets, the Fourier amplitudes, $\hat{\rho}_{\mathbf{k},\Re}$, of their averages density profiles, are shown for the first 9 wavevectors.

The average density profiles for the spherical and cylindrical droplets, obtained using equilibrium simulations, are shown in Figure 5b as a function of the radial coordinate in the pertinent coordinate system. The radius of the spherical droplet is 4.84 nm, and that of the cylindrical droplet is 3.17 nm; the axis of the cylindrical droplet is along the $z$-direction and its length is $L_z = 15$ nm. In contrast with planar slabs, all three wavevector-components must be considered to capture the particle density fields of the spherical and cylindrical droplets. A comparison of the Fourier amplitudes, $\hat{\rho}_{\mathbf{k},\Re}$, of these density fields is shown in Figures 5c and 5d for the first few wavevectors. For the spherical droplet, the $(1,0,0)$, $(0,1,0)$ and $(0,0,1)$ wavevectors display the largest signal with the $\hat{\rho}_{\mathbf{k},\Re}$-values for the three wavevectors being the same due to spherical symmetry; similarly, the $\hat{\rho}_{\mathbf{k},\Re}$-values for $(1,1,0)$, $(1,-1,0)$, $(1,0,1)$, $(1,0,-1)$, $(0,1,1)$ and $(0,1,-1)$ wavevectors are the same, but with a somewhat smaller magnitude. We note that by definition, $\hat{\rho}_{\mathbf{k},\Re} = \hat{\rho}_{-\mathbf{k},\Re}$ (Equation 5), so that

$\hat{\rho}_{\mathbf{k},\Re}$ must be the same for the $(1,0,0)$ and $(-1,0,0)$ wavevectors; however, this is not true for the $(1,1,0)$ and $(1,-1,0)$ wavevectors, i.e., $\hat{\rho}_{\mathbf{k},\Re}$ can, in general, be different for these wavevectors. With the axis of the cylindrical droplet pointing along the $z$-direction, the $\hat{\rho}_{\mathbf{k},\Re}$-values of the $(1,0,0)$ and $(0,1,0)$ wavevectors are identical (and display the largest signal), whereas the $(0,0,1)$ wavevector (along $z$) does not contribute to the density field; similarly, the $(1,1,0)$ and the $(1,-1,0)$ wavevectors contribute to the density field, but the $(1,0,1)$, $(1,0,-1)$, $(0,1,1)$ and $(0,1,-1)$ wavevectors do not. Thus, for the spherical and cylindrical droplets, the largest contrast in their $\hat{\rho}_{\mathbf{k},\Re}$-values is observed for the $(0,0,1)$ wavevector, with significant contrast additionally being observed for the $(1,0,1)$, $(1,0,-1)$, $(0,1,1)$ and $(0,1,-1)$ wavevectors. We thus bias these five wavevectors to sample the transition between the spherical and cylindrical droplets.

To obtain the free energetics of the transition, we perform a series of biased simulations that follow a linear path between the spherical and cylindrical droplet basins in the five-dimensional $\{\hat{\rho}_{\mathbf{k},\Re}\}$-space, as described in the Methods section. The simulations are performed with the system initialized as either a spherical droplet ("forward") or a cylindrical droplet ("backward"). We find that the free energetics of the transition, $F(\lambda)$, are independent of the initial state of the system (Figure 6a), suggesting that the transition can be sampled reversibly, and that any barriers in unbiased (orthogonal) degrees of freedom are comparable to the thermal energy (or smaller). Two minima are observed in $F(\lambda)$ near $\lambda = 0$ and 1, corresponding to the spherical and cylindrical droplets, respectively, with former being favored by $2.50 \pm 0.81\ k_{\mathrm{B}}T$. We note that this estimate does not include the free energetic cost of turning the bias on at $\lambda^* = 0$ and turning it off at at $\lambda^* = 1$, but as with the cleaving of the planar liquid slab, we expect these contributions to be relatively small. Using our density profiles and geometric expressions for the surface area of a sphere and a cylinder (excluding the cylindrical end-caps due to periodic boundaries), we estimate the surface areas of the spherical and cylindrical droplets to be 294.4 $\mathrm{nm}^2$ and 298.8 $\mathrm{nm}^2$, respectively. Upon multiplying the difference in interfacial area by the interfacial tension, we

obtain a free energy difference of 2.88 $k_{\mathrm{B}}T$, which is in good agreement with our simulated estimate of $2.50 \pm 0.81$ $k_{\mathrm{B}}T$.

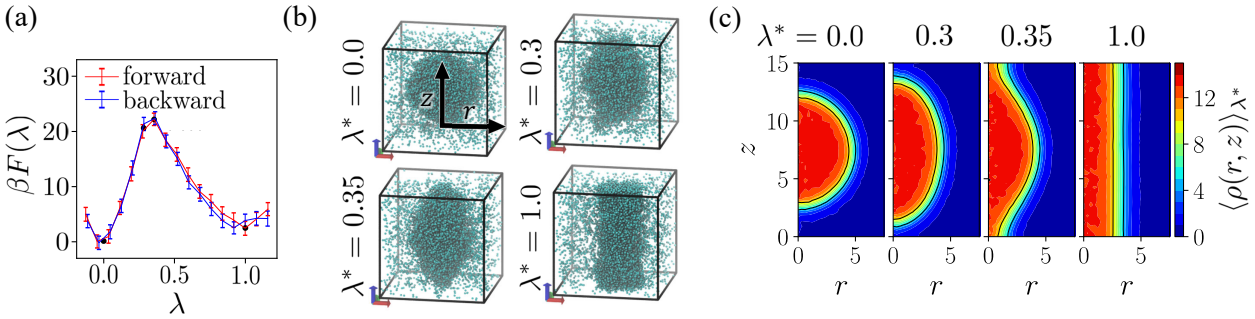


Figure 6: (a) By biasing the Fourier amplitudes, $\hat{\rho}_{\mathbf{k},\Re}$ of only 5 wavevectors, we are able to reversibly sample the transition from a spherical to a cylindrical droplet, and estimate the corresponding free energy, $F(\lambda)$. (b) Representative biased simulation snapshots for select $\lambda^*$-values. The $z-$ and $r-$axes of the cylindrical coordinate system, used to average particle densities, are shown in the top-left snapshot. (c) Averaged particle densities, $\langle \rho(r,z) \rangle_{\kappa,\lambda^*}$, obtained from select biased simulations. From left to right, the spherical droplet ($\lambda^* = 0$) stretches along the $z$-axis ($\lambda^* = 0.3$) until it contacts its periodic image ($\lambda^* = 0.35$), eventually forming a cylindrical droplet ($\lambda^* = 1$).

The minima in $F(\lambda)$ are separated by a barrier of roughly 20 $k_{\mathrm{B}}T$ at $\lambda = 0.35$. Typical configurations from biased simulations near the barrier, shown in Figure 6b, suggest that the transition state is an elongated ellipsoidal droplet that is about to contact itself across periodic boundaries. To shed further light into the transition pathway, we plot the particle density fields, observed in our biased simulations, as a function of the axial, $z$, and the radial, $r \equiv \sqrt{x^2 + y^2}$, coordinates (Figure 6c). We find that the transition pathway is characterized by the gradual elongation of the spherical droplet along the $z$-direction (for $\lambda^*$ near 0), followed by the formation of an unduloid-like shape (near $\lambda^* = 0.35$) when the droplet meets itself across periodic boundaries and eventually transitions into a cylindrical droplet (for $\lambda^*$ approaching 1). Importantly, these results suggest that biasing a small number of wavevectors may be sufficient to reversibly sample transitions between morphologies with different symmetries.

# Conclusions and Outlook

Molecular simulations promise to shed light on the intricate relationships between the molecular characteristics of building blocks and the conditions under which they might self-assemble into certain mesophases. However, free energy barriers can hinder self-assembly and/or supramolecular transitions, making it challenging to observe them in unbiased atomistic or coarse-grained simulations.[55–58] To address this challenge, here we propose biasing order parameters based on Fourier transforms of particle densities, $\hat{\rho}_{\mathbf{k}}$, which concisely capture the periodicity and symmetry of self-assembled structures. To illustrate our approach, we first characterize the free energy for clustering ideal gas particles, whose simplicity lends itself to analytical solutions that validate our results and guide our intuition.

Leveraging the ability of $\hat{\rho}_{\mathbf{k}}$ to discriminate between configurations with different periodicities, we then cleave a Lennard-Jones liquid slab into two slabs by simultaneously biasing the $\hat{\rho}_{\mathbf{k}}$-values for select wavevectors. In particular, we first bias $\hat{\rho}_{\mathbf{k}}$-values for 12 wavevectors, which contribute the most to the density profiles in the two basins, along a linear path connecting the two basins. We find that sampling of the cleavage transition is not hindered by the presence of orthogonal barriers, enabling robust estimation of the corresponding free energy as well as the liquid-vapor interfacial tension. Interestingly, we further find that biasing $\hat{\rho}_{\mathbf{k}}$ for as few as two wavevectors enables reversible sampling of the transition. Moreover, we find that free energy barriers that must be overcome as the system moves between the one-slab and two-slab states are lower when $\hat{\rho}_{\mathbf{k}}$-values for fewer wavevectors are biased.

Finally, to interrogate the utility of our approach for studying supramolecular transitions between mesophases with different shapes and/or symmetries, we study the transition between spherical and cylindrical liquid droplets. By biasing $\hat{\rho}_{\mathbf{k}}$-values for a handful of judiciously chosen wavevectors, we are able to reversibly sample the sphere-cylinder transition, characterize the underlying free energy landscape, and shed light on the transition pathway. Our findings thus highlight the utility and versatility of $\hat{\rho}_{\mathbf{k}}$ as order parameters in concisely discriminating between diverse configurations with different periodicities or symmetries, and

provide heuristics for using these order parameters for accurately and efficiently sampling morphological transitions in self-assembled systems.

Although we make use of exceedingly simple model systems to interrogate the utility of our approach, we are hopeful that our work will serve as a crucial first step in the development of a robust and computationally efficient framework for exploring self-assembly and supramolecular transitions in more realistic molecular systems. For example, the self-assembly of surfactants to form micelles could be studied by biasing $\hat{\rho}_{\mathbf{k}}$ corresponding to the density of surfactant head-groups; similarly, block copolymer self-assembly could be facilitated by biasing $\hat{\rho}_{\mathbf{k}}$ for one of the polymer blocks. To investigate more complex processes, such as the combination of micelles or self-assembly of polymers near surfaces,[122–125] it may be useful to focus our bias potentials on a portion of the simulation box. We note that our approach should be useful for both atomistic and coarse-grained simulations (e.g., MARTINI models or dissipative particle dynamics), which are commonly used to investigate self-assembly.[126,127]

However, as the complexity of the systems under consideration increases, it may become necessary to bias $\hat{\rho}_{\mathbf{k}}$ for multiple densities and/or compositions. Moreover, realistic models may display slow relaxation along orthogonal coordinates (e.g., due to solvation barriers), thereby necessitating biasing of additional pertinent order parameters. To efficiently characterize the assembly landscape for such complex systems, our approach could be combined with other enhanced sampling techniques, such as sparse sampling[95] or the string method.[128] In addition to obtaining the free energetics of supramolecular transitions, our approach also promises to shed light on the corresponding mechanistic pathways and could also be used as a starting point for characterizing the kinetics of the transitions.[129,130] Such information may prove useful for understanding high-dimensional transition pathways or for constructing deep learning models that facilitate the inverse design of block copolymers.[131,132]

## Acknowledgments

Z.V. was supported by the U.S. Department of Energy (DOE), Office of Science, Office of Basic Energy Sciences, under Award Number DE-SC0021241. A.J.P. is grateful for financial support from the Alfred P. Sloan Research Foundation (FG-2017-9406) and the Camille and Henry Dreyfus Foundation (TC-19-033).

## References

(1) Safran, S.; Pincus, P.; Andelman, D. Theory of spontaneous vesicle formation in surfactant mixtures. *Science* **1990**, *248*, 354–356.

(2) Philp, D.; Stoddart, J. F. Self-assembly in natural and unnatural systems. *Angewandte Chemie International Edition in English* **1996**, *35*, 1154–1196.

(3) Whitesides, G. M.; Grzybowski, B. Self-assembly at all scales. *Science* **2002**, *295*, 2418–2421.

(4) Whitesides, G. M.; Boncheva, M. Beyond molecules: Self-assembly of mesoscopic and macroscopic components. *Proceedings of the National Academy of Sciences* **2002**, *99*, 4769–4774.

(5) Jain, S.; Bates, F. S. On the origins of morphological complexity in block copolymer surfactants. *Science* **2003**, *300*, 460–464.

(6) Glotzer, S. C.; Solomon, M. J. Anisotropy of building blocks and their assembly into complex structures. *Nature materials* **2007**, *6*, 557.

(7) Aizenberg, J.; Black, A. J.; Whitesides, G. M. Control of crystal nucleation by patterned self-assembled monolayers. *Nature* **1999**, *398*, 495–498.

(8) Zhou, S.; Chu, B. Assembled materials: polyelectrolyte–surfactant complexes. *Advanced Materials* **2000**, *12*, 545–556.

(9) Loudet, J.-C.; Barois, P.; Poulin, P. Colloidal ordering from phase separation in a liquid-crystalline continuous phase. *Nature* **2000**, *407*, 611–613.

(10) Hartgerink, J. D.; Beniash, E.; Stupp, S. I. Self-assembly and mineralization of peptide-amphiphile nanofibers. *Science* **2001**, *294*, 1684–1688.

(11) Zhang, S.; Marini, D. M.; Hwang, W.; Santoso, S. Design of nanostructured biological materials through self-assembly of peptides and proteins. *Current opinion in chemical biology* **2002**, *6*, 865–871.

(12) Cölfen, H.; Mann, S. Higher-order organization by mesoscale self-assembly and transformation of hybrid nanostructures. *Angewandte Chemie International Edition* **2003**, *42*, 2350–2365.

(13) Thorkelsson, K.; Bai, P.; Xu, T. Self-assembly and applications of anisotropic nanomaterials: A review. *Nano Today* **2015**, *10*, 48–66.

(14) Glotzer, S. C. Assembly engineering: Materials design for the 21st century (2013 pv danckwerts lecture). *Chemical Engineering Science* **2015**, *121*, 3–9.

(15) Drummond, C. J.; Fong, C. Surfactant self-assembly objects as novel drug delivery vehicles. *Current opinion in colloid & interface science* **1999**, *4*, 449–456.

(16) Tang, Z.; Wang, Y.; Podsiadlo, P.; Kotov, N. A. Biomedical applications of layer-by-layer assembly: from biomimetics to tissue engineering. *Advanced materials* **2006**, *18*, 3203–3224.

(17) Zhang, L.; Chan, J. M.; Gu, F. X.; Rhee, J.-W.; Wang, A. Z.; Radovic-Moreno, A. F.; Alexis, F.; Langer, R.; Farokhzad, O. C. Self-assembled lipid- polymer hybrid nanoparticles: a robust drug delivery platform. *ACS nano* **2008**, *2*, 1696–1702.

(18) Rösler, A.; Vandermeulen, G. W.; Klok, H.-A. Advanced drug delivery devices via

self-assembly of amphiphilic block copolymers. *Advanced drug delivery reviews* **2012**, *64*, 270–279.

(19) Nagarajan, R.; Ruckenstein, E. Theory of surfactant self-assembly: a predictive molecular thermodynamic approach. *Langmuir* **1991**, *7*, 2934–2969.

(20) Bowden, N.; Terfort, A.; Carbeck, J.; Whitesides, G. M. Self-assembly of mesoscale objects into ordered two-dimensional arrays. *Science* **1997**, *276*, 233–235.

(21) Huie, J. C. Guided molecular self-assembly: a review of recent efforts. *Smart Materials and Structures* **2003**, *12*, 264.

(22) Patel, A. J.; Balsara, N. P. Observing Nucleation Close to the Binodal by Perturbing Metastable Polymer Blends. *Macromolecules* **2007**, *40*, 1675–1683.

(23) Liu, Y.; Liu, B.; Nie, Z. Concurrent self-assembly of amphiphiles into nanoarchitectures with increasing complexity. *Nano Today* **2015**, *10*, 278–300.

(24) Venturoli, M.; Smit, B. Simulating the self-assembly of model membranes. *PhysChemComm* **1999**, *2*, 45–49.

(25) Wu, Z.; Wu, J. W.; Michaudel, Q.; Jayaraman, A. Investigating the Hydrogen Bond-Induced Self-Assembly of Polysulfamides Using Molecular Simulations and Experiments. *Macromolecules* **2023**, *56*, 5033–5049.

(26) Nagarajan, R. Molecular packing parameter and surfactant self-assembly: the neglected role of the surfactant tail. *Langmuir* **2002**, *18*, 31–38.

(27) Wu, Z.; Collins, A. M.; Jayaraman, A. Understanding Self-Assembly and Molecular Packing in Methylcellulose Aqueous Solutions Using Multiscale Modeling and Simulations. *Biomacromolecules* **2024**, *25*, 1682–1695.

(28) Jedlinska, Z. M.; Riggleman, R. A. Effects of Associative Interactions on the Phase Behavior of Complex Coacervates. *Macromolecules* **2024**, *57*, 4323–4334.

(29) Jonkheijm, P.; van der Schoot, P.; Schenning, A. P.; Meijer, E. Probing the solvent-assisted nucleation pathway in chemical self-assembly. *Science* **2006**, *313*, 80–83.

(30) Shen, C.-L.; Murphy, R. M. Solvent effects on self-assembly of beta-amyloid peptide. *Biophysical journal* **1995**, *69*, 640–651.

(31) Käfer, D.; Witte, G.; Cyganik, P.; Terfort, A.; Wöll, C. A comprehensive study of self-assembled monolayers of anthracenethiol on gold: Solvent effects, structure, and stability. *Journal of the American Chemical Society* **2006**, *128*, 1723–1732.

(32) Bochicchio, D.; Pavan, G. M. From cooperative self-assembly to water-soluble supramolecular polymers using coarse-grained simulations. *ACS nano* **2017**, *11*, 1000–1011.

(33) Hamblin, R. L.; Nguyen, N. Q.; DuBay, K. H. Selective solvent conditions influence sequence development and supramolecular assembly in step-growth copolymerization. *Soft Matter* **2022**, *18*, 943–955.

(34) Abuzaina, F. M.; Patel, A. J.; Mochrie, S.; Narayanan, S.; Sandy, A.; Garetz, B. A.; Balsara, N. P. Structure and Phase Behavior of Block Copolymer Melts near the Sphere-Cylinder Boundary. *Macromolecules* **2005**, *38*, 7090–7097.

(35) Dreher, M. R.; Simnick, A. J.; Fischer, K.; Smith, R. J.; Patel, A.; Schmidt, M.; Chilkoti, A. Temperature triggered self-assembly of polypeptides into multivalent spherical micelles. *Journal of the American Chemical Society* **2008**, *130*, 687–694.

(36) Bodnarchuk, M. I.; Kovalenko, M. V.; Heiss, W.; Talapin, D. V. Energetic and entropic contributions to self-assembly of binary nanocrystal superlattices: temperature as the structure-directing factor. *Journal of the American Chemical Society* **2010**, *132*, 11967–11977.

(37) Swartley, J. R.; Niblo, J.; Zhang, Z.; DuBay, K. H. Self-Assembly of 2D Viral Capsids with Oscillatory Interactions. *Biophysical Journal* **2019**, *116*, 570a.

(38) Patel, R. A.; Colmenares, S.; Webb, M. A. Sequence Patterning, Morphology, and Dispersity in Single-Chain Nanoparticles: Insights from Simulation and Machine Learning. *ACS Polymers Au* **2023**, *3*, 284–294.

(39) Wang, Y.; Xu, H.; Zhang, X. Tuning the amphiphilicity of building blocks: controlled self-assembly and disassembly for functional supramolecular materials. *Advanced materials* **2009**, *21*, 2849–2864.

(40) Damasceno, P. F.; Engel, M.; Glotzer, S. C. Predictive self-assembly of polyhedra into complex structures. *Science* **2012**, *337*, 453–457.

(41) Chao, H.; Riggleman, R. A. Inverse design of grafted nanoparticles for targeted self-assembly. *Molecular Systems Design & Engineering* **2018**, *3*, 214–222.

(42) Müller, M. Process-directed self-assembly of copolymers: Results of and challenges for simulation studies. *Progress in Polymer Science* **2020**, *101*, 101198.

(43) Zhu, H.; Fan, Z.; Yu, L.; Wilson, M. A.; Nagaoka, Y.; Eggert, D.; Cao, C.; Liu, Y.; Wei, Z.; Wang, X. et al. Controlling Nanoparticle Orientations in the Self-Assembly of Patchy Quantum Dot-Gold Heterostructural Nanocrystals. *Journal of the American Chemical Society* **2019**, *141*, 6013–6021.

(44) Webb, M. A.; Jackson, N. E.; Gil, P. S.; de Pablo, J. J. Targeted sequence design within the coarse-grained polymer genome. *Science Advances* **2020**, *6*, eabc6216.

(45) Bassani, C. L.; van Anders, G.; Banin, U.; Baranov, D.; Chen, Q.; Dijkstra, M.; Dimitriyev, M. S.; Efrati, E.; Faraudo, J.; Gang, O. et al. Nanocrystal Assemblies: Current Advances and Open Problems. *ACS Nano* **2024**, *18*, 14791–14840.

(46) Bharadwaj, S.; Niebuur, B.-J.; Nothdurft, K.; Richtering, W.; Vegt, N. F. A. v. d.; M. Papadakis, C. Cononsolvency of thermoresponsive polymers: where we are now and where we are going. *Soft Matter* **2022**, *18*, 2884–2909.

(47) Kyriakos, K.; Philipp, M.; Lin, C.-H.; Dyakonova, M.; Vishnevetskaya, N.; Grillo, I.; Zaccone, A.; Miasnikova, A.; Laschewsky, A.; Müller-Buschbaum, P. et al. Quantifying the Interactions in the Aggregation of Thermoresponsive Polymers: The Effect of Cononsolvency. *Macromolecular Rapid Communications* **2016**, *37*, 420–425.

(48) Fernández-Castro, B.; Méndez-Morales, T.; Carrete, J.; Fazer, E.; Cabeza, O.; Rodríguez, J. R.; Turmine, M.; Varela, L. M. Surfactant Self-Assembly Nanostructures in Protic Ionic Liquids. *The Journal of Physical Chemistry B* **2011**, *115*, 8145–8154.

(49) Wei, W. Hofmeister Effects Shine in Nanoscience. *Advanced Science* **2023**, *10*, 2302057.

(50) Ghosh, S.; Ray, A.; Pramanik, N. Self-assembly of surfactants: An overview on general aspects of amphiphiles. *Biophysical Chemistry* **2020**, *265*, 106429.

(51) Chakraborty, S.; Berac, C. M.; Urschbach, M.; Spitzer, D.; Mezger, M.; Besenius, P.; Speck, T. Predicting the Supramolecular Assembly of Amphiphilic Peptides from Comprehensive Coarse-Grained Simulations. *ACS Applied Polymer Materials* **2022**, *4*, 822–831.

(52) Mondal, J.; Mahanthappa, M.; Yethiraj, A. Self-Assembly of Gemini Surfactants: A Computer Simulation Study. *The Journal of Physical Chemistry B* **2013**, *117*, 4254–4262.

(53) Ghosh, A.; Haverick, M.; Stump, K.; Yang, X.; Tweedle, M. F.; Goldberger, J. E. Fine-Tuning the pH Trigger of Self-Assembly. *Journal of the American Chemical Society* **2012**, *134*, 3647–3650.

(54) Morimitsu, Y.; Browne, C. A.; Liu, Z.; Severino, P. G.; Gopinadhan, M.; Sirota, E. B.; Altintas, O.; Edmond, K. V.; Osuji, C. O. Spontaneous assembly of condensate networks during the demixing of structured fluids. *Proceedings of the National Academy of Sciences* **2024**, *121*, e2407914121.

(55) Shelley, J. C.; Shelley, M. Y. Computer simulation of surfactant solutions. *Current opinion in colloid & interface science* **2000**, *5*, 101–110.

(56) Klein, M. L.; Shinoda, W. Large-scale molecular dynamics simulations of self-assembling systems. *Science* **2008**, *321*, 798–800.

(57) Marrink, S. J.; Corradi, V.; Souza, P. C.; Ingolfsson, H. I.; Tieleman, D. P.; Sansom, M. S. Computational modeling of realistic cell membranes. *Chemical reviews* **2019**, *119*, 6184–6226.

(58) Sammalkorpi, M.; Sanders, S.; Panagiotopoulos, A. Z.; Karttunen, M.; Haataja, M. Simulations of Micellization of Sodium Hexyl Sulfate. *J. Phys. Chem. B* **2011**, *115*, 1403–1410.

(59) Lee, O.-S.; Cho, V.; Schatz, G. C. Modeling the self-assembly of peptide amphiphiles into fibers using coarse-grained molecular dynamics. *Nano letters* **2012**, *12*, 4907–4913.

(60) Müller, M. Studying amphiphilic self-assembly with soft coarse-grained models. *Journal of Statistical Physics* **2011**, *145*, 967–1016.

(61) Srinivas, G.; Discher, D. E.; Klein, M. L. Self-assembly and properties of diblock copolymers by coarse-grain molecular dynamics. *Nature materials* **2004**, *3*, 638.

(62) Iscen, A.; Kaygisiz, K.; Synatschke, C. V.; Weil, T.; Kremer, K. Multiscale Simulations of Self-Assembling Peptides: Surface and Core Hydrophobicity Determine Fibril Stability and Amyloid Aggregation. *Biomacromolecules* **2024**, *25*, 3063–3075.

(63) Park, J.; Thapar, V.; Choe, Y.; Padilla Salas, L. A.; Ramírez-Hernández, A.; de Pablo, J. J.; Hur, S.-M. Coarse-Grained Simulation of Bottlebrush: From Single-Chain Properties to Self-Assembly. *ACS Macro Lett.* **2022**, *11*, 1167–1173.

(64) Taddese, T.; Anderson, R. L.; Bray, D. J.; Warren, P. B. Recent advances in particle-based simulation of surfactants. *Current Opinion in Colloid & Interface Science* **2020**, *48*, 137–148.

(65) Lavagnini, E.; Cook, J. L.; Warren, P. B.; Hunter, C. A. Systematic Parameterization of Ion–Surfactant Interactions in Dissipative Particle Dynamics Using Setschenow Coefficients. *J. Phys. Chem. B* **2022**, *126*, 2308–2315.

(66) Santo, K. P.; Neimark, A. V. Dissipative particle dynamics simulations in colloid and Interface science: a review. *Advances in Colloid and Interface Science* **2021**, *298*, 102545.

(67) Del Regno, A.; Warren, P. B.; Bray, D. J.; Anderson, R. L. Critical Micelle Concentrations in Surfactant Mixtures and Blends by Simulation. *J. Phys. Chem. B* **2021**, *125*, 5983–5990.

(68) Shen, K.; Nguyen, M.; Sherck, N.; Yoo, B.; Köhler, S.; Speros, J.; Delaney, K. T.; Shell, M. S.; Fredrickson, G. H. Predicting surfactant phase behavior with a molecularly informed field theory. *Journal of Colloid and Interface Science* **2023**, *638*, 84–98.

(69) Müller, M.; Pablo, J. J. d. Computational Approaches for the Dynamics of Structure Formation in Self-Assembling Polymeric Materials. *Annual Review of Materials Research* **2013**, *43*, 1–34.

(70) Koski, J. P.; Ferrier, R. C. J.; Krook, N. M.; Chao, H.; Composto, R. J.; Frischknecht, A. L.; Riggleman, R. A. Comparison of Field-Theoretic Approaches in Predicting Polymer Nanocomposite Phase Behavior. *Macromolecules* **2017**, *50*, 8797–8809.

(71) Jacobs, W. M.; Reinhardt, A.; Frenkel, D. Communication: Theoretical prediction of free-energy landscapes for complex self-assembly. *The Journal of chemical physics* **2015**, *142*, 021101.

(72) Yu, T.; Schatz, G. C. Free energy profile and mechanism of self-assembly of peptide amphiphiles based on a collective assembly coordinate. *The Journal of Physical Chemistry B* **2013**, *117*, 9004–9013.

(73) Müller, M.; Daoulas, K. C. Calculating the free energy of self-assembled structures by thermodynamic integration. *The Journal of chemical physics* **2008**, *128*, 024903.

(74) Bussi, G.; Laio, A. Using metadynamics to explore complex free-energy landscapes. *Nature Reviews Physics* **2020**, *2*, 200–212.

(75) Barducci, A.; Bonomi, M.; Parrinello, M. Metadynamics. *WIREs Computational Molecular Science* **2011**, *1*, 826–843.

(76) Kästner, J. Umbrella sampling. *WIREs Computational Molecular Science* **2011**, *1*, 932–942.

(77) Patel, A. J.; Varilly, P.; Chandler, D.; Garde, S. Quantifying Density Fluctuations in Volumes of All Shapes and Sizes Using Indirect Umbrella Sampling. *Journal of Statistical Physics* **2011**, *145*, 265–275.

(78) Yang, Y.; Thyagarajan, R.; Ford, D. M.; Bevan, M. A. Dynamic colloidal assembly pathways via low dimensional models. *The Journal of chemical physics* **2016**, *144*, 204904.

(79) Tang, X.; Koenig, P. H.; Larson, R. G. Molecular Dynamics Simulations of Sodium Dodecyl Sulfate Micelles in Water The Effect of the Force Field. *The Journal of Physical Chemistry B* **2014**, *118*, 3864–3880.

(80) Wang, H.; Tang, X.; Eike, D. M.; Larson, R. G.; Koenig, P. H. Scission free energies for wormlike surfactant micelles: development of a simulation protocol, application, and validation for personal care formulations. *Langmuir* **2018**, *34*, 1564–1573.

(81) Shelley, J.; Watanabe, K.; Klein, M. L. Simulation of a sodium dodecylsulfate micelle in aqueous solution. *International Journal of Quantum Chemistry* **1990**, *38*, 103–117.

(82) Honeycutt, J. D.; Andersen, H. C. Molecular dynamics study of melting and freezing of small Lennard-Jones clusters. *Journal of Physical Chemistry* **1987**, *91*, 4950–4963.

(83) Larson, R. G. *The structure and rheology of complex fluids*; Oxford university press New York, 1999; Vol. 150.

(84) Keys, A. S.; Iacovella, C. R.; Glotzer, S. C. Characterizing structure through shape matching and applications to self-assembly. *Annu. Rev. Condens. Matter Phys.* **2011**, *2*, 263–285.

(85) Mai, Y.; Eisenberg, A. Self-assembly of block copolymers. *Chemical Society Reviews* **2012**, *41*, 5969–5985.

(86) Surewicz, W. K.; Mantsch, H. H.; Chapman, D. Determination of protein secondary structure by Fourier transform infrared spectroscopy: a critical assessment. *Biochemistry* **1993**, *32*, 389–394.

(87) Kim, S. O.; Solak, H. H.; Stoykovich, M. P.; Ferrier, N. J.; de Pablo, J. J.; Nealey, P. F. Epitaxial self-assembly of block copolymers on lithographically defined nanopatterned substrates. *Nature* **2003**, *424*, 411.

(88) Xu, B. Identifying fabric structures with fast Fourier transform techniques. *Textile Research Journal* **1996**, *66*, 496–506.

(89) Lindahl, E.; Edholm, O. Mesoscopic undulations and thickness fluctuations in lipid bilayers from molecular dynamics simulations. *Biophysical journal* **2000**, *79*, 426–433.

(90) Matsumoto, M.; Saito, S.; Ohmine, I. Molecular dynamics simulation of the ice nucleation and growth process leading to water freezing. *Nature* **2002**, *416*, 409.

(91) Sagui, C.; Darden, T. A. Molecular dynamics simulations of biomolecules: long-range electrostatic effects. *Annual review of biophysics and biomolecular structure* **1999**, *28*, 155–179.

(92) Pedersen, U. R. Statistics of small length scale density fluctuations in supercooled viscous liquids. *The Journal of chemical physics* **2019**, *150*, 094505.

(93) Invernizzi, M.; Valsson, O.; Parrinello, M. Coarse graining from variationally enhanced sampling applied to the Ginzburg–Landau model. *Proceedings of the National Academy of Sciences* **2017**, *114*, 3370–3374.

(94) Pampel, B.; Valsson, O. Improving the Efficiency of Variationally Enhanced Sampling with Wavelet-Based Bias Potentials. *Journal of Chemical Theory and Computation* **2022**, *18*, 4127–4141.

(95) Xi, E.; Remsing, R. C.; Patel, A. J. Sparse sampling of water density fluctuations in interfacial environments. *Journal of chemical theory and computation* **2016**, *12*, 706–713.

(96) Xi, E.; Marks, S. M.; Fialoke, S.; Patel, A. J. Sparse sampling of water density fluctuations near liquid-vapor coexistence. *Molecular Simulation* **2018**, *44*, 1124–1135.

(97) Tan, Z.; Gallicchio, E.; Lapelosa, M.; Levy, R. M. Theory of binless multi-state free energy estimation with applications to protein-ligand binding. *The Journal of Chemical Physics* **2012**, *136*.

(98) Zhu, F.; Hummer, G. Convergence and error estimation in free energy calculations using the weighted histogram analysis method. *Journal of Computational Chemistry* **2012**, *33*, 453–465.

(99) Shirts, M. R.; Chodera, J. D. Statistically optimal analysis of samples from multiple equilibrium states. *The Journal of Chemical Physics* **2008**, *129*, 124105.

(100) Hess, B.; Kutzner, C.; Van Der Spoel, D.; Lindahl, E. GROMACS 4: algorithms for highly efficient, load-balanced, and scalable molecular simulation. *Journal of chemical theory and computation* **2008**, *4*, 435–447.

(101) Frenkel, D.; Smit, B. *Understanding Molecular Simulations: From Algorithms to Applications*, 2nd ed.; Academic Press: New York, 2002.

(102) Bussi, G.; Donadio, D.; Parrinello, M. Canonical sampling through velocity rescaling. *The Journal of chemical physics* **2007**, *126*, 014101.

(103) Kästner, J.; Thiel, W. Bridging the gap between thermodynamic integration and umbrella sampling provides a novel analysis method: "Umbrella integration". *The Journal of Chemical Physics* **2005**, *123*, 144104.

(104) Kirkwood, J. G. Statistical Mechanics of Fluid Mixtures. *The Journal of Chemical Physics* **1935**, *3*, 300–313.

(105) Binder, K.; Block, B. J.; Virnau, P.; Tröster, A. Beyond the van der Waals loop: What can be learned from simulating Lennard-Jones fluids inside the region of phase coexistence. *American Journal of Physics* **2012**, *80*, 1099–1109.

(106) Brugarolas, T.; Tu, F.; Lee, D. Directed assembly of particles using microfluidic droplets and bubbles. *Soft Matter* **2013**, *9*, 9046–9058.

(107) Sarker, D. K. Engineering of Nanoemulsions for Drug Delivery. *Current Drug Delivery* **2005**, *2*, 297–310.

(108) Lv, C.; Hao, P.; Zhang, X.; He, F. Dewetting Transitions of Dropwise Condensation on Nanotexture-Enhanced Superhydrophobic Surfaces. *ACS Nano* **2015**, *9*, 12311–12319.

(109) Syms, R. R.; Yeatman, E. M.; Bright, V. M.; Whitesides, G. M. Surface tension-powered self-assembly of microstructures-the state-of-the-art. *Journal of Microelectromechanical systems* **2003**, *12*, 387–417.

(110) Ismagilov, R. F.; Schwartz, A.; Bowden, N.; Whitesides, G. M. Autonomous movement and self-assembly. *Angewandte Chemie International Edition* **2002**, *41*, 652–654.

(111) Srinivasan, U.; Liepmann, D.; Howe, R. T. Microstructure to substrate self-assembly using capillary forces. *Journal of microelectromechanical systems* **2001**, *10*, 17–24.

(112) Leong, T. G.; Lester, P. A.; Koh, T. L.; Call, E. K.; Gracias, D. H. Surface tension-driven self-folding polyhedra. *Langmuir* **2007**, *23*, 8747–8751.

(113) Kirkwood, J. G.; Buff, F. P. The statistical mechanical theory of surface tension. *The Journal of Chemical Physics* **1949**, *17*, 338–343.

(114) Ghoufi, A.; Malfreyt, P.; Tildesley, D. J. Computer modelling of the surface tension of the gas–liquid and liquid–liquid interface. *Chemical Society Reviews* **2016**, *45*, 1387–1409.

(115) Sun, L.; Li, X.; Hede, T.; Tu, Y.; Leck, C.; Ågren, H. Molecular dynamics simulations of the surface tension and structure of salt solutions and clusters. *The Journal of Physical Chemistry B* **2012**, *116*, 3198–3204.

(116) Chen, L.-J. Area dependence of the surface tension of a Lennard-Jones fluid from molecular dynamics simulations. *The Journal of chemical physics* **1995**, *103*, 10214–10216.

(117) Gloor, G. J.; Jackson, G.; Blas, F. J.; de Miguel, E. Test-area simulation method for the direct determination of the interfacial tension of systems with continuous or discontinuous potentials. *The Journal of chemical physics* **2005**, *123*, 134703.

(118) Vega, C.; de Miguel, E. Surface tension of the most popular models of water by using the test-area simulation method. *The Journal of chemical physics* **2007**, *126*, 154707.

(119) Remsing, R. C.; Xi, E.; Patel, A. J. Protein hydration thermodynamics: The influence of flexibility and salt on hydrophobin ii hydration. *The Journal of Physical Chemistry B* **2018**, *122*, 3635–3646.

(120) Irving, J.; Kirkwood, J. G. The statistical mechanical theory of transport processes. IV. The equations of hydrodynamics. *The Journal of chemical physics* **1950**, *18*, 817–829.

(121) Velinova, M.; Sengupta, D.; Tadjer, A. V.; Marrink, S.-J. Sphere-to-Rod Transitions of Nonionic Surfactant Micelles in Aqueous Solution Modeled by Molecular Dynamics Simulations. *27*, 14071–14077, Publisher: American Chemical Society.

(122) Deshmukh, S. A.; Solomon, L. A.; Kamath, G.; Fry, H. C.; Sankaranarayanan, S. K. Water ordering controls the dynamic equilibrium of micelle–fibre formation in self-assembly of peptide amphiphiles. *Nature communications* **2016**, *7*, 1–11.

(123) Zou, W.; Tan, G.; Jiang, H.; Vogtt, K.; Weaver, M.; Koenig, P.; Beaucage, G.; Larson, R. G. From well-entangled to partially-entangled wormlike micelles. *Soft matter* **2019**, *15*, 642–655.

(124) Segal-Peretz, T.; Ren, J.; Xiong, S.; Khaira, G.; Bowen, A.; Ocola, L. E.; Divan, R.; Doxastakis, M.; Ferrier, N. J.; de Pablo, J. et al. Quantitative Three-Dimensional Characterization of Block Copolymer Directed Self-Assembly on Combined Chemical and Topographical Prepatterned Templates. *ACS Nano* **2017**, *11*, 1307–1319.

(125) Sambasivam, A.; Sangwai, A. V.; Sureshkumar, R. Self-Assembly of Nanoparticle–Surfactant Complexes with Rodlike Micelles: A Molecular Dynamics Study. *Langmuir* **2016**, *32*, 1214–1219.

(126) Hoogerbrugge, P.; Koelman, J. Simulating microscopic hydrodynamic phenomena with dissipative particle dynamics. *EPL (Europhysics Letters)* **1992**, *19*, 155.

(127) Huo, Z.; Skala, S. J.; Falck, L. R.; Laaser, J. E.; Statt, A. Computational Study of Mechanochemical Activation in Nanostructured Triblock Copolymers. *ACS Polym. Au* **2022**, *2*, 467–477.

(128) Weinan, E.; Ren, W.; Vanden-Eijnden, E. Simplified and improved string method for computing the minimum energy paths in barrier-crossing events. *Journal of Chemical Physics* **2007**, *126*, 164103.

(129) Gleria, I.; Mocskos, E. E.; Tagliazucchi, M. E. Minimum Free-Energy Paths for the Self-Organization of Polymer. **2017**,

(130) Jacobs, W. M.; Reinhardt, A.; Frenkel, D. Rational design of self-assembly pathways for complex multicomponent structures. *Proceedings of the National Academy of Sciences* **2015**, *112*, 6313–6318.

(131) Reinhart, W. F.; Statt, A. Opportunities and Challenges for Inverse Design of Nanostructures with Sequence Defined Macromolecules. *Acc. Mater. Res.* **2021**, *2*, 697–700.

(132) Moghimi, E.; Chubak, I.; Ntetsikas, K.; Polymeropoulos, G.; Wang, X.; Carillo, C.; Statt, A.; Cipelletti, L.; Mortensen, K.; Hadjichristidis, N. et al. Interpenetrated and Bridged Nanocylinders from Self-Assembled Star Block Copolymers. *Macromolecules* **2024**, *57*, 926–939.

# TOC Graphic